Biobased hydrogel nanocomposite containing modified cellulosic nanofiber-ZnO nanohybrid

Highlights

This chapter describes the fabrication of a nanohybrid based on modified cellulose nanofiber and zinc oxide nanoparticles using an eco-friendly and non-toxic approach. The nanohybrid was then incorporated into a starch/itaconic acid/acrylic acid-based hydrogel matrix. The formation of the nanohybrid and its successful incorporation into the hydrogel matrix were studied by different microscopic and spectroscopic techniques. The obtained hydrogel nanocomposites (HNCs) were employed for removal of metal ions from their aqueous solutions, manifested noteworthy adsorption ability. The adsorption kinetics and isotherm studies were investigated to understand the metal ion removal mechanism. Moreover, reusability of the HNC was tested for up to three repeated cycles without noticing any significant efficiency. Additionally, to observe the effect of nanohybrid, biodegradability of the HNC was performed and compared with the bare hydrogel matrix.

Parts of this chapter are published as

[1] Bora, A., Sarmah, D., and Karak, N. Bio-based biodegradable hydrogel containing modified cellulosic nanofiber-ZnO nanohybrid as efficient metal ions removers with recyclable capacity. *Journal of Cleaner Production*, 430:139748, 2023.

5.1. Introduction

Currently, as discussed in the **Chapter 4,** adsorption methods are considered as a promising method for wastewater treatment because of their effectiveness, convenience, ease of operation as well as economic and environmental reasons [1]. Among various adsorbents such as fly ash, synthetic polymer resin, activated carbon, silica, etc., hydrogel has been recognized by the scientific community as an excellent adsorbent for wastewater remediation. As described in **Chapter 4,** hydrogels are three-dimensional networks with highly porous structures. They can absorb species both within the network and on the surface of the material. Due to high-water swelling capacity, hydrogel has great potential in wastewater treatment [2]. In recent years, industrial development and human activities have released large amounts of heavy metal ions such as copper, arsenic, nickel, lead, etc. into the aquatic environment which can cause severe health and environmental damages to ecosystems through phytotoxicity, carcinogenicity, and facile bioaccumulation along with the contamination of food chain [3,4]. To address this issue, many scientific efforts have been made to develop biobased hydrogel nanocomposites (HNCs) using polysaccharides such as starch, chitosan, cellulose, etc. along with the incorporation of nanostructured materials to obtain hydrogels with radiant characteristics including multifunctionality, high porosity, surface area, etc. Various nano-dimensional metal oxides such as manganese oxide, iron oxide, aluminum oxide, magnesium oxide, etc. has been extensively used to improve the adsorption capacity of bare hydrogel matrix [5,6]. Because of their nanoscale dimension, nanomaterials (NMs) have a high surface area to volume ratio, resulting in additional sites for removal of various metal ions on the surface of hydrogel nanocomposites (HNCs) [7,8]. Among various metal oxides, zinc oxide (ZO) nanoparticles (NPs) have received the attention of many researchers. Due to its antibacterial and antifungal effects, ZO has great potential for applications in sensing, biology, medicine, etc., besides removing metal ions from wastewater. Recently, synthesis of ZO NMs via ecofriendly routes have attracted great interest from researchers due to its high stability, low production cost, adsorption capacity, and naturally friendly nature [9].

As discussed in **Chapter 1,** the development of metal oxide nanohybrids based on a supporting material is one of the most promising and rapidly developing research areas in materials chemistry these days [10,11]. Nanohybrids are defined as combinations of inorganic, organic components, or intimate mixtures of both types of components, which

synergistically enhance the performance of the resulting materials [10]. Metals or metal oxides NPs are known to be unstable due to their large specific surface areas and tend to agglomerate during synthesis. Therefore, many researchers have developed NPs by using suitable supporting substrates such as cellulose nanofibers (CNFs), which is associated with excellent properties including non-toxicity, environmental friendliness, cheap biodegradability, biocompatibility, and ease of fabrication [12]. Fortunately, CNFs have numerous surface hydroxyl groups that are stable in water and are easy to modify by physical adsorption of other chemical species or by chemical synthesis, making them a green template or support material for the fabrication of nanohybrid materials. Therefore, stabilization of metal or metal oxide NPs using CNFs as green templates might be the most effective way to mitigate aggregation [13].

Here, we describe an ecofriendly method for synthesis of nanohybrid based on ZO NPs and CNFs using thuja leaf extract as a bio-reductant and fabrication of nanohybrid incorporated starch-, itaconic acid (IA), acrylic acid (AA)-based HNCs through an *in-situ* polymerization process. Here, the nanohybrid was prepared by using an ecofriendly route with wastepaper derived CNF as supporting material for ZO NPs. The prepared nanohybrid and HNCs were characterized using various analytical techniques. Further, water swelling profile and removal of Cu(II) and Fe(II) ions from aqueous media was studied using the prepared HNCs. To attain the maximum adsorption capacity (q_e) of HNCs toward the metal ions, adsorption studies including the effects of nanohybrid amount, adsorbent dosage, temperature, contact time, pH and initial metal concentration were conducted. Additionally, the adsorption kinetics and isotherms were examined. For biodegradation, the soil burial test was also performed for HNCs.

5.2. Experimental section

5.2.1. Materials

Starch, IA, AA, ammonium persulfate (APS), N,N'-methylene bis-acrylamide (MBA), and NaOH were used with similar quality and specifications as mentioned in **Chapter 2.** Aqueous dispersion of modified-cellulose nanofiber (mCNF) was obtained by using the same procedure as mentioned in **Chapter 4.**

Further, thuja (*Thuja Oreantalis*) leaves were collected from the premises of Department of Chemical Sciences, Tezpur University, India and used in NMs preparations.

Zinc nitrate ($Zn(NO_3)_2$) (molar mass 189.36 g/mol), ferric chloride ($FeCl_3$) (molar mass 162.20 g/mol), copper sulfate ($CuSO_4$) (molar mass 159.62 g/mol), and ferrous chloride

($FeCl_2$) (molar mass 126.75 g/mol) were purchased from Merck, India and used as received.

5.2.2. Methods

5.2.2.1. Preparation of aqueous *Thuja Oreantalis* leaf phytoextract

To prepare the aqueous plant extract, 5 g of freshly collected *Thuja Oreantalis* leaves were cleaned and air-dried at room temperature. Next, the leaves were ground roughly with a domestic mixture grinder and 2 g of these ground leaves were boiled for 1 h at 60 °C in 50 mL of distilled water. After cooling to room temperature, the extract was collected by centrifugation. Finally, the extract was stored in a refrigerator for further experiments [14].

5.2.2.2. Biosynthesis of modified-cellulose nanofiber/zinc oxide nanohybrid (ZONH)

In this work, ZONH was prepared with some modifications to the previously described method [15]. In the procedure, 0.2 M ethanolic solution of $Zn(NO_3)_2$ (5 mL) was added dropwise to ethanolic NaOH solution (35 mL), and a milky white precipitate was formed. Then 5 mL of mCNF aqueous dispersion containing 15 mg mL^{-1} solid content was added and stirred vigorously. Further, the mixture was sonicated for 10 min to completely mix the reactants. The mixture was then refluxed with 10 mL of thuja leaf extract and two-three drops of freshly prepared $FeCl_3$ solution (0.01 M) at 80 °C for 2 h. After cooling the solution to room temperature, the resulting light brown precipitate was cleaned with water to remove the remaining zinc species and other byproducts and then collected by centrifugation at 3,000 rpm for 10 min. Finally, the reduced $Zn(OH)_2$-mCNF was transformed into ZONH by vacuum drying at 60 °C overnight.

5.2.2.3. Synthesis of ZONH reinforced HNC

In this work, ZONH reinforced HNC was prepared using the method as described in **Chapter 2** with some modifications. Briefly, a fixed amount of starch and IA were dissolved in 10 mL of aqueous NaOH (0.067N) solution and fully gelatinized at 80-90 °C using a three-neck round bottom flask, equipped with nitrogen gas flow and a mechanical stirrer. The mixture was then kept for a while until the temperature reached 60 °C, after which a certain amount of AA was added to the mixture along with 1 mL of water. At this moment, an aqueous solution containing 1 mL of water with MBA as a cross-linking agent and a desired amount of ZONH dispersion (0, 0.15 and 0.25 wt%) was added into the above homogeneous solution, and stirred for 10 min. Consequently, a

certain amount of APS was added to the mixture and polymerized under N_2 atmosphere until a solid gel like product was formed. Finally, the product was taken out, washed thoroughly with methanol and dried at 70 °C. The ground hydrogel powder was then used for further studies. Also, for comparison, a bare hydrogel was prepared by the same method as discussed in **Chapter 2**. The formulations of the synthesized hydrogel samples are shown in **Table 5.1**.

Table 5.1. Compositions of prepared ZONH loaded HNCs.

Hydrogel	Starch (g)	IA (g)	AA (g)	APS (g)	MBA (g)	ZONH (wt%)
HNC0	1	0.1	0.9	0.04	0.01	0
HNC1	1	0.1	0.9	0.04	0.01	0.15
HNC2	1	0.1	0.9	0.04	0.01	0.25

5.2.2.4. Structural analysis

Various analytical technique including Fourier transform infrared (FTIR), X-ray diffraction (XRD), field emission scanning electron microscopy (FESEM) and dynamic light scattering (DLS) were used for analysis and their instrumental details are described in **Chapter 2, Chapter 3** as well as **Chapter 4**. The UV absorption spectra were recorded using the same UV spectrophotometer as mentioned in **Chapter 2.** Further, energy dispersive X-ray (EDX) spectrophotometer attached to scanning electron microscopy (SEM) (JEOL, Japan, JSM 6390LV model) was used to confirm the elemental composition. The same atomic absorption spectrophotometer (AAS) was used to determine the amount of metal ions as mentioned in **Chapter 3.**

5.2.2.5. Water swelling capacity measurement

To determine the water swelling profile, the water absorption capacity (WAC) of the HNCs was measured by using **Eq 2.1 as** mentioned in **Chapter 2**.

5.2.2.6. Metal ion adsorption test

To observe the effect of ZONH content on adsorption, we studied the adsorption capacity of HNCs. For this purpose, 0.01 g of each HNC was added to 50 mL of 20 ppm metal ion solutions. Afterwards, optimal composition was selected as a typical sample and batch adsorption test was performed.

Tests were conducted in 100 mL beakers with 0.005-0.02 g of HNC added to 50 mL of metal ion solutions (20-60 ppm) ranging in pH from 4 to 9. The solutions were stirred at 150 rpm at different temperatures (30-50 °C) by a magnetic stirrer. The solution pH was

adjusted using 0.1 M HCl or NaOH solution. After completion of the test, HNC was separated by filtration, and the metal ion concentrations before and after uptake were measured by AAS. Then, the q_e (mg g^{-1}) value was determined by using **Eq. 4.3** of **Chapter 4** and removal percentage (%) were determined by using the following equation [16].

$$\text{Removal (\%)} = \frac{c_0 - c_e}{c_0} \times 100 \text{ ------- (Eq 5.1)}$$

where c_o and c_e indicate the concentrations metal ions (in ppm) before and after adsorption.

5.2.2.7. Kinetic model

To study the mechanisms of the metal ions adsorption process, 0.01 g of adsorbent was added to 50 mL of Cu(II) and Fe(II) solutions, and stirred continuously. After pre-determined time intervals, amounts of metal ions remaining in the solution were measured using **Eq. 4.3** of **Chapter 4**. The pseudo-first-order (PFO) (**Eq. 5.2**) and pseudo-second-order (PSO) models (**Eq. 5.3**) were applied to describe the adsorption kinetics of metal ions on HNC [17].

$$log(q_e - q_t) = log\, q_e - \frac{k_1 t}{2{\cdot}303} \text{-------(Eq. 5.2)}$$

$$\frac{t}{q_t} = \frac{1}{k_2 q_e^2} + \frac{t}{q_e} \text{----------(Eq. 5.3)}$$

where k_1 (min^{-1}) and k_2 (g $mg^{-1}min^{-1}$) indicate the rate constant for the PFO and PSO model, respectively. The term q_e and q_t are the quantities of metal ions removed after equilibrium and predetermined time t, respectively.

5.2.2.8. Adsorption isotherm experiment

Adsorption isotherms of Cu(II) and Fe(II) metal ions on HNC was conducted by batch experiments in which 0.01 g of HNC was mixed with 50 mL of varying concentrations of metal ions from 20 to 60 ppm. After 30 min of adsorption, residual metal ions were measured using **Eq. 4.3** of **Chapter 4**. The equilibrium data acquired from adsorption studies were applied to the Langmuir and Freundlich isotherms models, which are given in **Eq. 5.4** and **Eq. 5.5** [17].

$$\frac{C_e}{q_e} = \frac{Ce}{q_m} + \frac{1}{q_m} K_L \text{ --------- (Eq. 5.4)}$$

$$log\, q_e = log\, k_f + \frac{1}{n} log\, C_e$$ ---------**(Eq. 5.5)**

where q_e and C_e denote the amount of removed metal ions per g of HNC and concentration of metal ion solution after equilibrium, respectively, q_m designates the maximum amount of metal ions adsorbed per g of HNC, and K_L is the Langmuir constant. K_F and n indicate the Freundlich constant and adsorption intensity, respectively. Specifically, n represents the adsorption efficiency and degree of surface heterogeneity. For instance, n values greater than 1 suggest favorable adsorption.

5.2.2.9. Reusability experiment

In this work, adsorption/desorption cycles were performed to study the recyclability of HNC. Initially, 0.01 g of HNC was placed in a tea bag and stirred in 50 mL of metal ion solutions (20 ppm) for 30 minutes. The quantity of metal ions removed was measured by AAS according to **Eq. 4.3** of **Chapter 4**. To regenerate the adsorbent, metal ion desorption studies were carried out by conducting the metal ion adsorbed by HNC on a magnetic stirrer in 50 mL of 0.1 M HCl solution at 50 °C for 1 h. After removing the adsorbent from the desorption medium, the quantity of metal ions released into the medium was calculated. The HNC was then washed with deionized water and finally poured into 0.1 M NaOH solution and kept on the magnetic stirrer for another 1 h. To test the reusability of the HNC, the processes of metal ion adsorption-desorption cycles were carried out up to three times using the same HNC. The quantity of desorbed metal ion was calculated from the equation given below [18].

$$\text{Desorption (\%)} = \frac{B}{A} \times 100$$ --------**(Eq. 5.6)**

where A and B indicate the concentration of metal ions adsorbed on HNC and desorbed to the elution medium, respectively.

5.2.2.10. Biodegradation test

A soil burial test was conducted to evaluate the biodegradability of the prepared HNC using the method as described in **Chapter 2**. However, in this case, the test was carried out for both HNC and bare hydrogel matrix and 6 sets of samples for each HNC were considered. Further, the test was carried out for 35 days and estimated the percent weight loss using **Eq. 2.11** of **Chapter 2**.

5.3. Results and discussion

5.3.1. Synthesis of ZONH

Nowadays, phytochemicals are used for biosynthesis of NPs. These phytochemicals are antioxidants, free of toxic chemicals and possess excellent capacity to reduce metal ions and stabilize them at the nanoscale [19]. Therefore, plant extracts act simultaneously as stabilizing and reducing agents. In this work, thuja leaf extract containing compounds with hydroxyl and carbonyl group was used as a stabilizing and complexing agent that might be responsible for the formation of ZO NPs [20]. Further, CNFs obtained from wastepaper have been used in the formation of mCNFs via carboxymethylation as discussed in **Chapter 4**. The prepared mCNFs with carboxylate groups (COO^-) were also utilized as green template for stabilization of ZO NPs which have been found to attach to the mCNFs surface via electrostatic interactions [13]. Since CNF is renewable and ZO is less reactive and less toxic, therefore, preparation of ZONH from mCNF and ZO using phytoextract is assumed to be sustainable. It is found that prepared ZONH can be easily dispersible in water. A simple scheme representing the used steps to generate ZONH is displayed in **Scheme 5.1**.

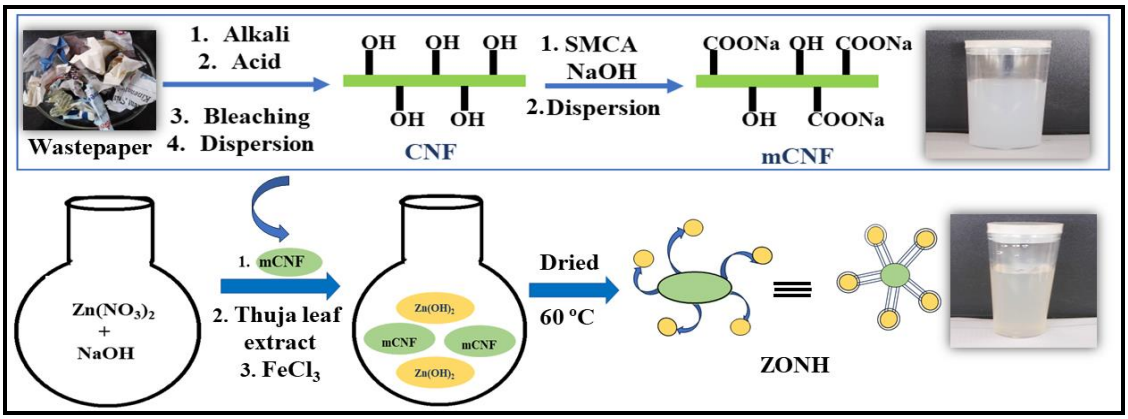

Scheme 5.1. Schematic illustration of preparation of mCNF and synthesis of ZONH.

5.3.2. Preparation of HNCs

A general schematic representation for the synthesis of HNCs via a radical copolymerization reaction is shown in **Scheme 5.2**. The mechanism of HNC synthesis is described with the support of **Chapter 2**. First, APS is thermally decomposed at 70 ^oC to produce anionic sulfate radicals. Such generated radicals react with the primary OH groups of starch to produce alkoxy macroradicals. These macroradicals can attack the vinyl groups of AA and IA by directly initiating the graft copolymerization and forming a three dimensionally cross-linked network structure for the hydrogel, as the graft copolymer chains simultaneously coupled with both the ends of the MBA vinyl group to

form a three-dimensional network. Further, ZONH are assumed to be present on the surface of hydrogel network via physical and electrostatic interactions which can be confirmed from the analysis part of the proceeding section.

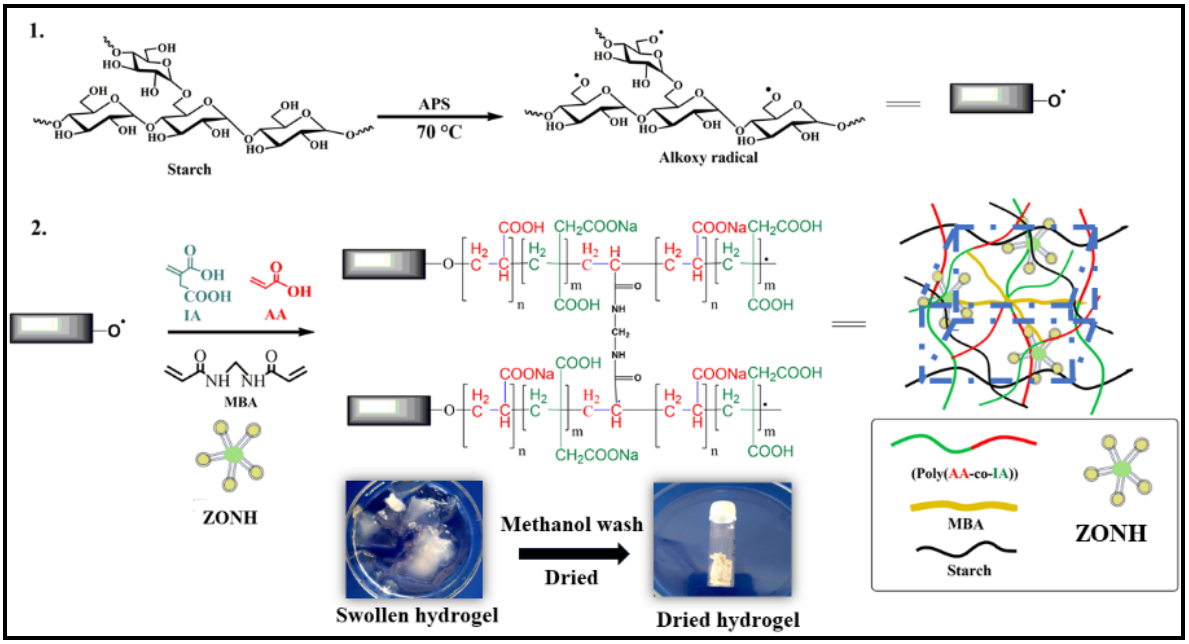

Scheme 5.2. Schematic illustration of the formation of the ZONH reinforced HNC.

5.3.3. Characterization

5.3.3.1. UV-visible spectral analysis

The UV-Visible absorption spectra of ZO and ZONH are shown in **Figure 5.1.a**. It displayed a broad peak at 350 nm that matched the characteristic band of ZO NPs [21].

5.3.3.2. FTIR analysis

The FTIR spectroscopy was used to characterize the synthesized ZO, ZONH and HNC. From the FTIR spectra of ZO and ZONH shown in **Figure 5.1.b**, we find that a characteristic peak of the Zn-O stretching vibration emerges at 556 cm^{-1} in the FTIR spectra of both ZO and ZONH [22]. In addition, several additional peaks of different functional groups have been recognized in both the spectra. A wide peak around 3427 cm^{-1} was obtained which can be ascribed to O-H stretching vibration of the phenolic/carboxyl group of the plant extract. Moreover, the peak around 1618 cm^{-1} and 1410 cm^{-1} can be ascribed to C=C ring stretching in polyphenols and bending vibrations of O-H in carboxyl groups, respectively. Further, a peak around 1030 cm^{-1} (C-O-C stretching frequency) was also observed [23].

Figure 5.1.c. shows the FTIR spectra of the prepared HNCs. As shown in **Figure 5.1.c**, the absorption band of the O-H stretching vibration at 3427 cm^{-1} and the characteristic peaks at 2915 and 2854 cm^{-1} indicate the O-H, C–H asymmetry and symmetry stretching vibrations of starch, IA and AA present in the hydrogel matrix [24]. Further, the spectra show a peak at 1022 cm^{-1} indicating stretching vibration of the glycosidic C-O-C linkages in the starch backbone. Similarly, the C=O band of COOH and COO^- groups of AA and IA were observed at 1721 and 1630 cm^{-1}, respectively [25]. These results can be attributed to the successful grafting of AA and IA on the starch. Moreover, in addition to the above peaks, we also found that a peak at 573 cm^{-1} was retained only for HCN1 and HCN2, but not present in HNC0. This may be due to Zn-O stretching vibrations arising from the presence of ZONH in the HNCs [26]. Thus, characteristic peaks in the FTIR spectra support the formation of ZONH and indicate the presence of ZONH within the hydrogel matrix.

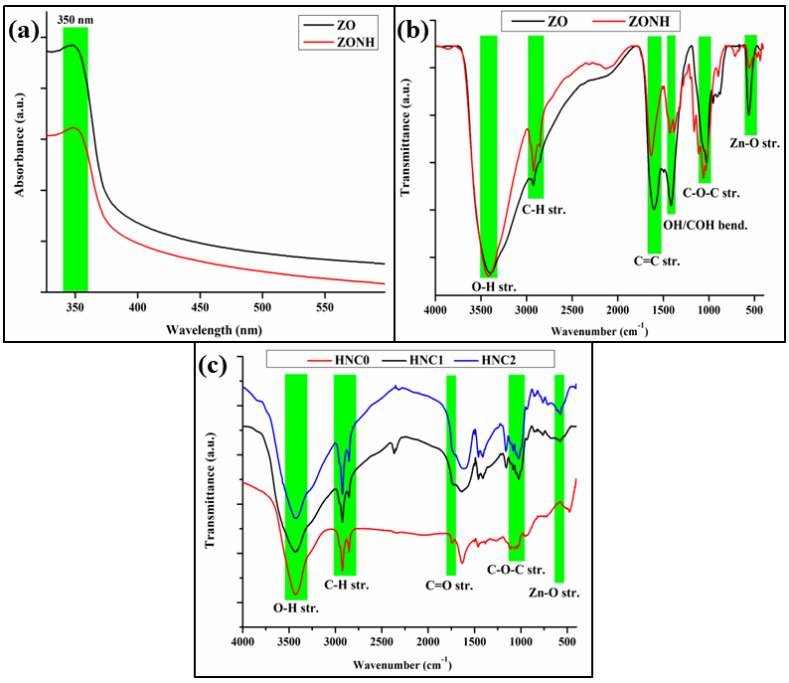

Figure 5.1. (a) UV-visible spectra of ZO and ZONH and FTIR spectra of (b) ZO, ZONH; and (c) HNC0, HNC1, HNC2.

5.3.3.3. XRD analysis

The XRD patterns of mCNF, ZO and the corresponding ZONH are shown in **Figure 5.2.a**. The characteristic broad peak at 22.23° corresponds to the (002) crystallographic plane, which is the characteristic peaks of mCNF. XRD analysis of the synthesized ZO NPs revealed characteristic peaks at 31.56°, 34.11°, 36.02°, 47.29°, 56.11°, 62.56°, 66.04°, 67.79°, 68.91°, 72.09° and 76.70° of (100), (002), (101), (102), (110), (103),

(200), (112), (201), (004) and (202) crystal lattice planes, correspondingly. These peaks are consistent with the previously reported observations of ZO NPs [27]. Moreover, the presence of all the characteristic low-intensity peaks of ZO along with the peak at 22.23° corresponding to mCNF confirmed the presence of those peaks in the synthesized ZONH. It is also confirmed that the synthesized nanohybrid do not contain any characteristic peaks other than mCNF and ZO peaks.

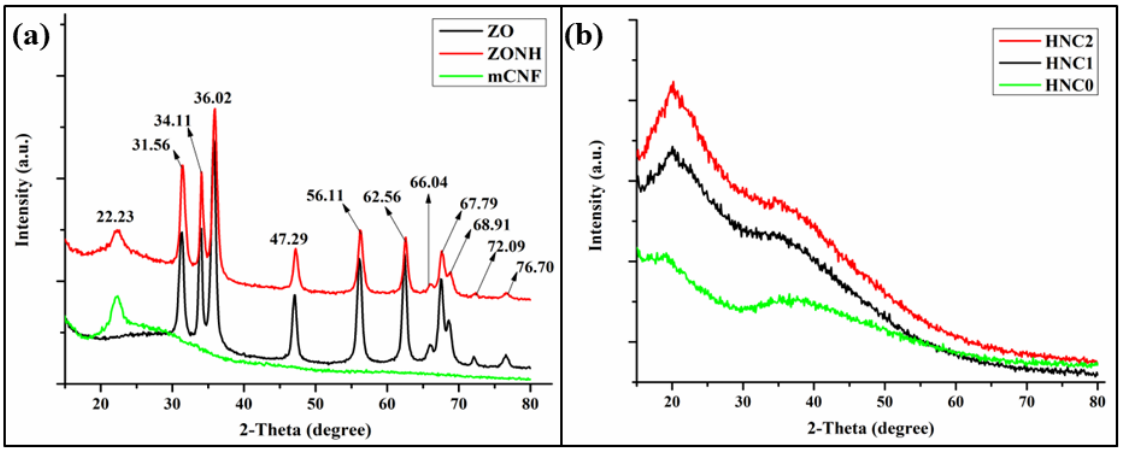

Figure 5.2. XRD patterns of (a) ZO, mCNF and ZONH; and (b) HNC0, HNC1 and HNC2.

Furthermore, we observed the structural changes in HNCs using the XRD technique. XRD patterns of HNCs with different ZONH contents were obtained, as shown in **Figure 5.2.b**. XRD pattern of bare hydrogel (HNC0) without ZONH shows broad peaks around 20.3 and 35.1°, indicating its amorphous nature. However, the intensity of the peak at 2θ = 20.3° for HNC1 and HNC2 was found to be relatively higher, indicating higher crystallinity than HNC0. Thus, difference in peak intensities of HNC0, HNC1 and HNC2 can be ascribed to the presence of ZONH on the surface of HNC, and we found that the crystallinity increased with the ZONH content from 0.15 to 0.25 wt%.

5.3.3.4. EDX analysis

EDX spectra were recorded to determine the surface elemental compositions and their weight percentage of ZONH and HNC2 as shown in **Figure 5.3.(a** and **b)**. EDX analysis indicated that ZONH (**Figure 5.3.a.**) contains about 61.12% of zinc, 27.26% of oxygen, 9.03% of carbon, and 2.60% of nitrogen. The spectra show two distinct peaks for zinc at 1 and 8.7 keV and one significant peak at about 0.5 keV for oxygen, which are characteristic of ZO NPs [28]. The high peak intensities of zinc and oxygen indicate that the majority of the synthesized nanohybrid are ZO. Moreover, the EDX spectrum of

HNC2 (**Figure 5.3.b.**) indicated 2.16% of zinc, 51.01% of oxygen, 41.78 % of carbon and 5.06% of sodium were present in the matrix. Thus, as shown in **Figure 5.3.b**, the EDX spectrum confirmed the presence of only Zn, O, C and N with no other impurity elements in the samples.

5.3.3.5. Dynamic light scattering (DLS)

Regardless of size and shape, either DLS or TEM should be used for reliable size measurements of NPs [27]. In this study, the particle size distribution of biosynthesized ZONH and mCNF was determined using DLS method. The number size distribution of mCNF and ZONH particles in water are shown in **Figure 5.3.(c** and **d)**. Average particle sizes of 70 and 126 nm were found for ZONH and mCNF, correspond to 17.1 and 18% respectively of the total volume of sample analyzed, respectively.

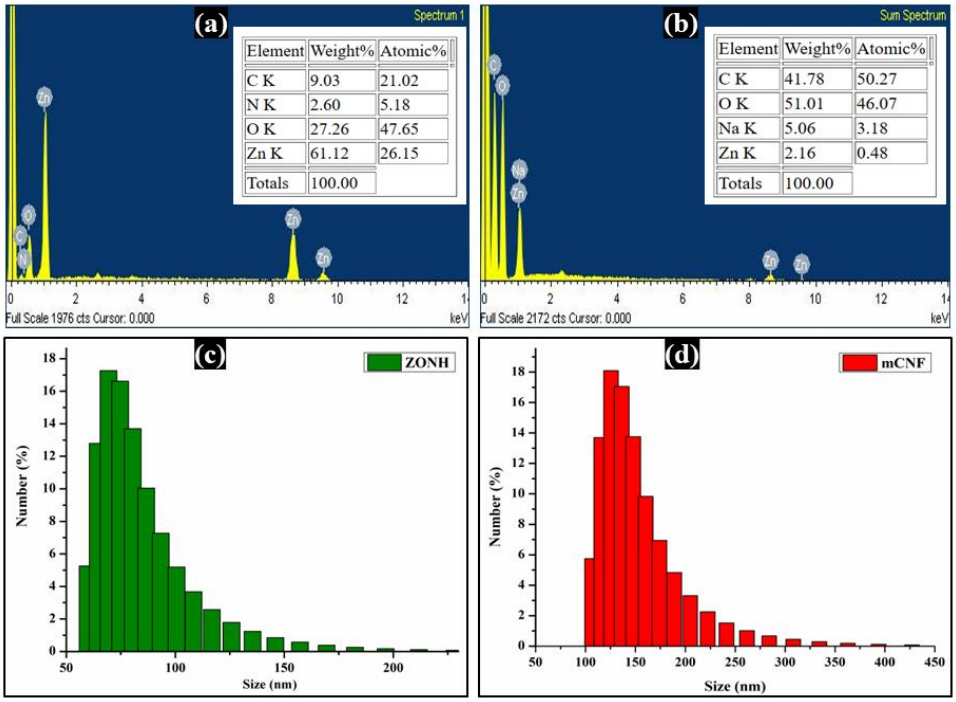

Figure 5.3. Typical EDX spectra of (a) ZONH and (b) HNC containing ZONH content of 0.25 wt%. Number against size distribution of (c) ZONH and (d) mCNF.

5.3.3.6. FESEM analysis

FESEM analysis was utilized to observe the surface morphologies of the synthesized ZO, ZONH and HNC2 and **Figure 5.4.** displays the resulting images. From **Figure 5.4.a**, it can be observed that ZO NPs are mostly in the nanometer scale with an average diameter of less than 100 nm. The ZO NPs are slightly aggregated, which is distinctive for green synthesis-based NPs, in general. This occurs because biosynthetic NPs have large surface

areas and strong affinities that lead to aggregation. As a result, the NPs attach to each other throughout the formation process and spontaneously form structures with different shapes [27]. Further, FESEM images at high magnification of synthesized ZONH showed that CNFs induced flowerlike clusters of nanohybrids which can be seen on the surface of mCNF as shown in **Figure 5.4.(b** and **c)** at two different magnifications [29]. However, their flowerlike shapes are irregular in nature. From these results, it can be concluded that the presence of ZO NPs on the surface of mCNF resulted in the formation of the ZONH.

Moreover, FESEM images in **Figure 5.4.(d** and **e)** showed the porous structure of HNC2 which is considered to be advantageous for its swelling as well as adsorption properties and possible rapid adsorption kinetics [30]. Further, **Figure 5.4.f**. shows the rough surface of HNC2 at higher magnification, indicating that the nanohybrids are well dispersed on the surface of HNC2. This can be attributed to the presence of electrostatic stabilization between residual carboxyl groups of the ZONH and the functional groups of HNC matrix [31]. Also, from the EDX spectrum (**Figure 5.3.b.)**, it can be concluded that ZONH was obtained on the surface of HNC2, and the corresponding FESEM images of the samples were verified.

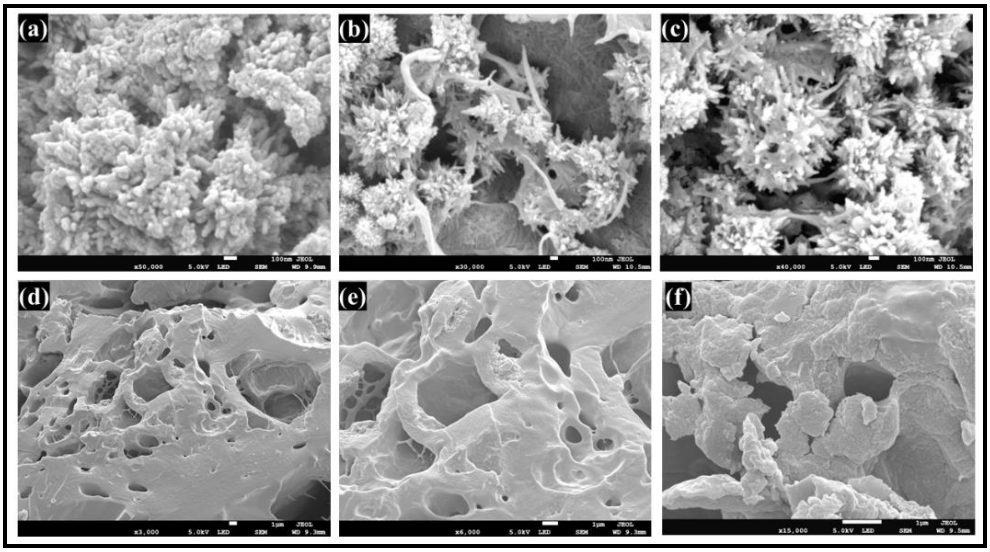

Figure 5.4. FESEM images of as-obtained (a) ZO at 50,000X magnification (100 nm scale), ZONH at (b) 30,000X (100 nm scale) and at (c) 50,000X (100 nm scale) magnification. HNC2 at (d) 3000X (1μm scale), (e) 6000X (1μm scale) and (f) 15,000X (1μm scale) magnifications.

5.3.4. Water swelling study

Figure 5.5.a. displays the WAC values of HNCs as a function of time. The figure shows that the WAC for all samples is high, reaches an equilibrium state during the first 40

min, and that as time goes on, there is a small variation in the values. The maximum equilibrium WACs for HNC0, HNC1 and HNC2 with 0, 0.15 and 0.25 wt% ZONH were found to be 509, 538 and 580 g/g, respectively. Since the absorption behavior depends on the presence of functional groups in the hydrogel network structure, so, hydrogels with more ionizable groups have better swelling capacity [32]. In this case, the presence of starch, AA and IA results in high WAC. The cause for this ability is that they contain highly hydrophilic –OH and $–COO^-$ groups. Further, increasing the amount of ZONH from 0.15 to 0.25% increases the water uptake capacity. This is likely due to the effect of ZONH being present. Since, ZONH is composed of ZO and mCNF, in which mCNF contains a hydrophilic ionizable carboxyl functional group and is deprotonated in distilled water, resulting in electrostatic repulsion between carboxyl groups within the network structure of the hydrogel causing more osmotic pressure differences that leads to the sufficiently swelling of the hydrogel [31]. Therefore, ZO-embedded HNCs possessed slightly higher WAC compared to the pristine hydrogel i.e., HNC0.

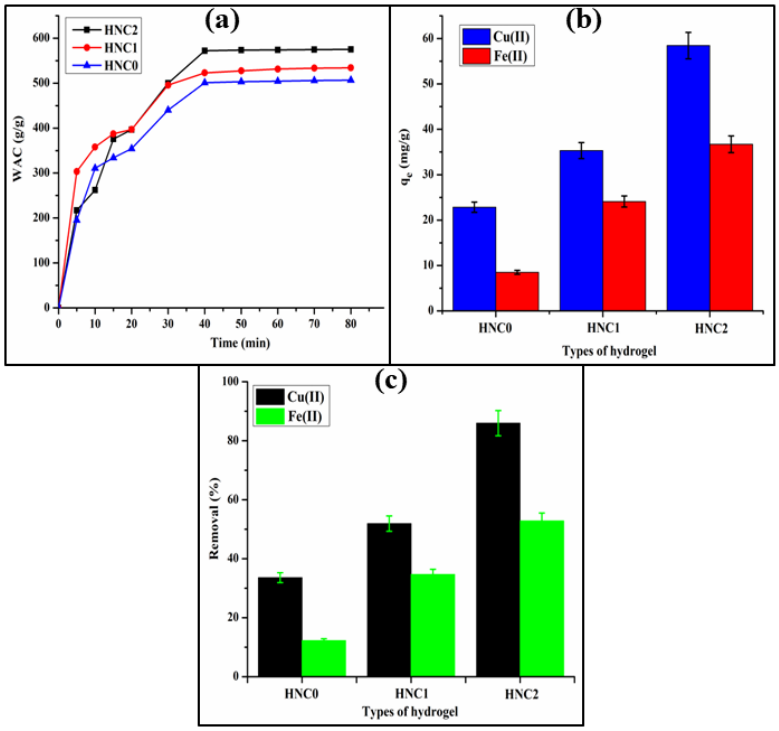

Figure 5.5. (a) Water swelling profiles of HNCs. Effect ZONH content on (b) adsorption capacity and (c) removal percentage of HNCs for Cu(II) and Fe(II) ions.

The above result suggests that HNC2 with ZONH content of 0.25 wt% is the best within the range explored template for metal ion adsorption, since high WAC and rapid absorption equilibrium properties are important parameters for water purification hydrogels as adsorbents.

5.3.5. Metal ion adsorption

Initially, we have investigated the effect of ZONH on metal ion removal capacity and the results are shown in **Figure 5.5.(b** and **c)**. From the figure, we find that as the amount of ZONH in the HNC material increases, the metal ion removal efficiency increases with respect to both removal percentage and adsorption capacity. As shown in **Figure 5.5.b,** the highest q_e values of HNC2 reinforced with ZONH content of 0.25 wt% were found to be 58 mg g^{-1} and 37 mg g^{-1} for Cu(II) and Fe(II) ions, respectively. Similarly, HNC2 also showed the highest metal ion removal (%), 86% for Cu(II) ions and 54% for Fe(II) ions (**Figure 5.5.c.).** This behavior can be assigned to the electrostatic interactions that exist between the cationic metal ions and negative charges of the HNC [33]. The presence of negatively charged -COO^- groups on ZONH and hydrogel matrix can be attributed to their enhanced adsorption capacity towards positively charged metal ions via electrostatic interactions, complex formation, etc. [32]. Therefore, a high adsorption capacity value was observed for HNC2 loaded with a ZONH content of 0.25 wt%. The results also showed that the samples without ZONH i.e., HNC0 could not effectively remove metal ions from the solution compared to HNC1 and HNC2. Therefore, increasing the amount of ZONH in HNC promoted the adsorption of metal ions.

Thus, the highest uptake of metal ions was obtained for HNC2 loaded with a ZONH content of 0.25 wt%. Therefore, HNC2 was selected as a typical sample for further investigation of Cu(II) and Fe(II) in order to obtain optimized condition for the highest removal capacity.

5.3.5.1. Effect of contact time

To study the effect of time on the q_e values of the prepared adsorbent, adsorption time ranging from 2 to 50 min were investigated at room temperature. **Figure 5.6.a**. shows the time-dependent adsorption curves of the metal ions by HNC2. The adsorption was found to be proceeded quickly and nearly reach equilibrium within 30 min indicating a high diffusion rate of the metal ions inside the hydrogel. Therefore, a contact time of 30 min was chosen as the optimal contact time to achieve the q_e values in the following experiments. After this time, adsorption was found to be slowed down and reached almost to the equilibrium state. This is due to the high number of adsorption sites available for adsorption in the early stages [33]. However, the remaining available adsorption sites become increasingly difficult to access over time.

Additionally, a higher saturated adsorption capacity of HNC2 for Cu(II) was observed compared to Fe(II) with the same ionic valence number. This can be attributed to the small size of Cu(II). An earlier study found that the smaller the radius, the faster the metal ion adsorption process [32]. Therefore, higher saturated adsorption capacity is observed for Cu(II) ions than Fe(II) ions.

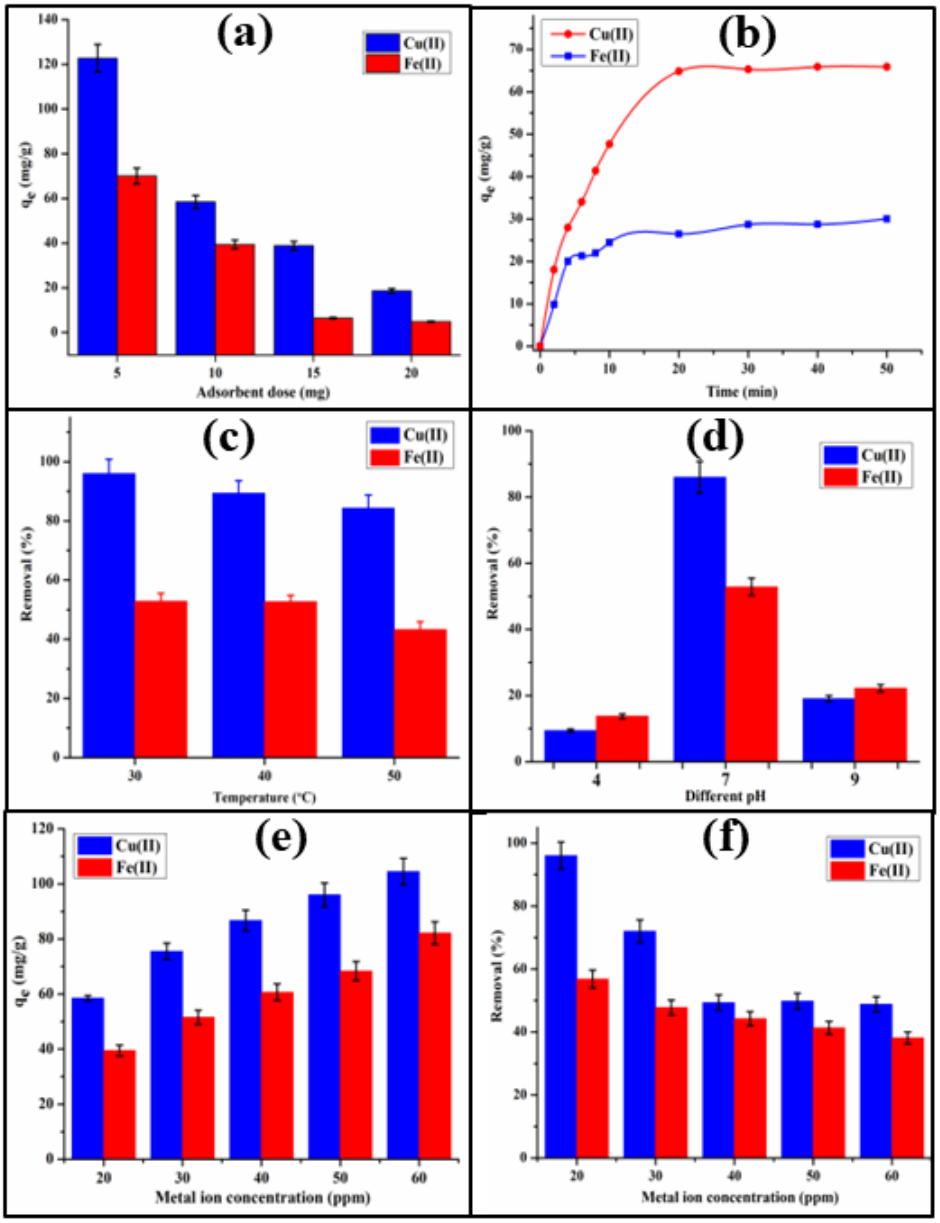

Figure 5.6. Effect of (a) contact time; (b) adsorbent dose, (c) temperature, (d) pH on adsorption capacity of HNC2 for Cu(II) and Fe(II) ion; and effect of initial metal ion concentration of HNC2 on (e) adsorption capacity and (f) removal percentage for Cu(II) and Fe(II).

5.3.5.2. Effect of adsorbent dose

Determining the optimal amount of adsorbent is a crucial step in achieving the q_e value of an adsorbent [34]. Therefore, in this case, the effect of adsorbent dosage for metal ion

removal was investigated for amounts of HNC from 5 to 20 mg and results are shown in **Figure 5.6.b**. The figure shows that the adsorption capacity for Cu(II) and Fe(II) ions decreases as the amount of adsorbent increases. The q_e value for Cu(II) and Fe(II) was found to be 122 and 70 mg g^{-1} with adsorbent dosage of 0.005 g. From these results it can be said that with the increasing adsorbent dosage at a certain metal ion concentration, all the active adsorption sites of HNC2 cannot be covered by metal ions and equilibrium was not reached. Therefore, active surface sites on the adsorbent remained unsaturated. Thus, for both Cu(II) and Fe(II) ions, the highest metal ion uptake was achieved with 0.005 g of sorbent.

5.3.5.3. Effect of temperature

Figure 5.6.c. illustrates how temperature affects the ability of HNC2 to adsorb metal ions. It was observed that highest metal ion uptake capacity was obtained at 30 °C and then uptake capacity was found to be decrease with the increasing temperature from 30 to 50 °C. This may be because of weakening of binding forces between the active sites on the hydrogel and the metal ions with increasing temperature. The reason might be a drop-in surface activity, which indicates that the adsorption process between metal ions and adsorbent is exothermic [35].

5.3.5.4. Effect of pH

Further, pH of the testing media also significantly effects on metal ion removal capacity of adsorbent. Therefore, to study how the pH of the solution affects the removal of Fe(II) and Cu(II) ions, 0.01 g of HNC2 was separately added to 50 mL of solution containing 20 ppm of metal ions at different pH values, from 4 to 9. From **Figure 5.6.d,** it can be seen that the q_e value is remarkably affected by the initial pH of the solution, reaching the q_e value at an initial pH of 7. Below pH 7, the HNC2 exhibits low adsorption ability for Fe(II) and Cu(II) ions. This is likely due to competition for adsorption between H^+ and the metal ions. It is evident that metal ions with high concentrations and small ionic radii are adsorbed preferably [30]. Therefore, in strongly acidic solutions, the ability of carboxyl groups to chelate Cu(II) and Fe(II) ions reduced, and only a small quantity of metal ions were removed at pH 4. However, as the pH increased, the amount of H^+ ions reduced gradually and thus, negatively charged adsorption sites of HNC2 increased, which enhanced the metal ions uptake ability. From this, it can be concluded that at pH 7, ionization of the –COOH group occurred, yielding the negatively charged HNC.

Therefore, electrostatic attraction becomes the dominant force between metal ions and the HNC. As a result, the q_e value of metal ions was obtained at pH 7. However, above the pH value of 7, production of excess Na^+ ions generate a screening effect which in turn leads to the reduction in adsorption of metal ions. Thus, the lower uptake of metal ions was obtained at pH 9 compared to pH 7. Hence, an optimal pH 7 was chosen for the adsorption tests.

5.3.5.5. Effect of initial metal ion concentration

One more experiment was performed at room temperature to observe the effect of initial metal ion concentration. To carry out this experiment, the metal ion concentration was changed from 20 to 60 ppm and both adsorption capacity and adsorption percentage are shown in **Figure 5.6.e** and **Figure 5.6.f**, respectively. It was found that the q_e value increased from 58 to 104 for Cu(II) and 39 to 82 mg/g for Fe(II) as the initial metal ion concentration increased from 20 to 60 ppm. This is probably because the concentration gradient of the metal ions increases the driving force when metal ion concentration increases and promotes the diffusion of the metal ions on the HNC2 [36]. However, the removal percentage of metal ions decreased from 96 to 48% for Cu(II) ions and 56 to 38% for Fe(II) ions.

5.3.6. Kinetic study

In order to study the mechanism of the adsorption process, adsorption kinetics were also studied. As was already mentioned, the kinetics of the adsorption process is crucial when designing adsorption systems for practical applications [37]. For this purpose, PFO and PSO were used to study the kinetics and mechanisms of sorption of Cu(II) and Fe(II) ions on the prepared adsorbents, and the best model for the experimental kinetic data was chosen. The plots of the two kinetic models for the two metal ions are shown in **Figure 5.7.(a** and **b)** and corresponding parameters are determined using **Eq. 5.2** and **Eq. 5.3**, which are summarized in **Table 5.2**.

Moreover, the results in **Table 5.2** indicate that the adsorption of metal ions on HNC2 is consistent with the PSO model since the correlation coefficient (R^2) obtained for HNC2 as adsorbent was close to unit via the PSO kinetic model. Moreover, the model shows that the theoretical adsorption capacities ($q_{e,cal}$) and the experimental adsorption capacities ($q_{e,exp}$) are in nearly good agreement compared to the PFO model. This result thus suggests that the adsorption of Fe(II) and Cu(II) ions onto the adsorbent involves

chemical interaction between the hydrogel surface and the metal ions which dominates the adsorption process [33].

Table 5.2. Kinetic parameters for adsorption of Cu(II) and Fe(II) on the HNC2 adsorbent.

	Pseudo first order kinetics			
Sample	**k_1 (min^{-1})**	**q_{exp} (mg g^{-1})**	**q_{cal} (mg g^{-1})**	**R^2**
Cu(II)	0.1676	58	108.45	0.93719
Fe(II)	0.0634	39	18.22	0.86312
	Pseudo second order kinetics			
Sample	**K_2 (g $mg^{-1}min^{-1}$)**	**q_{exp} (mg g^{-1})**	**q_{cal} (mg g^{-1})**	**R^2**
Cu(II)	$2.29x10^{-3}$	58	76.16	0.98829
Fe(II)	$9.09x10^{-3}$	39	31.81	0.99759

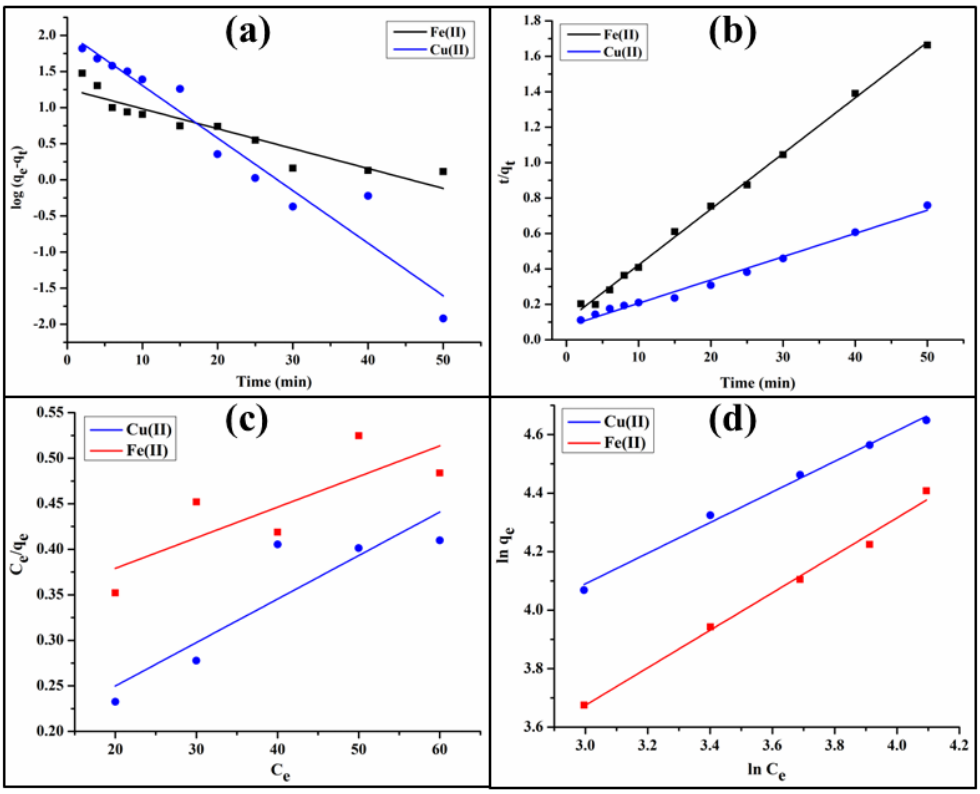

Figure 5.7. (a) The PFO and (b) PSO model fitting curves (Contact time: 2-50 min, pH: 7, adsorbent dosage: 0.010 g, initial concentration: 20 ppm). (c) The Langmuir and (d) Freundlich isotherms (Initial concentration: 20-60 ppm, pH: 7, adsorbent dosage: 0.010 g, contact time: 30 min).

5.3.7. Adsorption isotherm study

Adsorption isotherm studies are commonly carried out to investigate what types of interactions are present between adsorbates and adsorbents [32]. The two adsorption

isotherms for HNC2 towards Cu(II) and Fe(II) ions are shown in **Figure 5.7.(c** and **d)**. When plotting the results with the two isotherm models, it was found that the value of R^2 (given in **Table 5.3)** for the Freundlich isotherm was closer to unit, showing a more linear pattern compared to the value for the Langmuir isotherm. The results revealed that Freundlich model fits to the adsorption data better than the Langmuir model. This indicates that the adsorption of both the metal ions occurs in multilayers on the heterogeneous surface of HNC2.

Further, the value (1/n) in Freundlich adsorption isotherm denotes the favorability of adsorption process. Thus, adsorption process is considered favorable if the value of 1/n lies between the range of 0.1 to 1, and it is a chemical process if the value of n is less than 1 [38]. Otherwise, adsorption is a physical process. In this study, **Table 5.3** shows that the 1/n values for both Cu(II) and Fe(II) range from 0.1 to 1, indicating that chemisorption is the preferred adsorption process.

Table 5.3. Isotherm's parameters for adsorption of Cu(II) and Fe(II) on the HNC2 adsorbent.

Parameters	**Cu(II)**	**Fe(II)**
Langmuir		
$q_{m,L}$(mg g^{-1})	209.2	297.61
K_L (L mg^{-1})	32.26	92.79
R^2	0.74806	0.54137
Freundlich		
K_F (L mg^{-1})	0.39698	0.5707
1/n	0.5236	0.64089
R^2	0.99158	0.98948

5.3.8. Metal ion adsorption-desorption study

Recoverability and recyclability of sorbents are not only important for environmental protection but also for cost, time and energy efficiency considerations. These qualities allow the adsorbent to successfully address the issues posed by waste generation and its production [34]. To study the reusability of HNC2, three cycles of adsorption and desorption experiments were performed. As shown in **Figure 5.8.a**, HNC2 as an adsorbent retains nearly 86% and 57% of their original q_e value for Cu(II) and Fe(II), respectively, even after three consecutive adsorption-desorption cycles. Moreover, **Figure 5.8.b**. shows that the desorption rate of Cu(II) ions decreased from 79.20% to

75.18% and that of Fe(II) ions decreased from 75.94% to 61.88% after 3 cycles. From these results, it can be concluded that the adsorbent might have poor desorption performance but maintains adsorption efficiency over 3 cycles for both metal ions. These results demonstrate that HNC2 can adsorb Cu(II) and Fe(II) ions over three cycles of adsorption and desorption without significant reduction in adsorption efficiency.

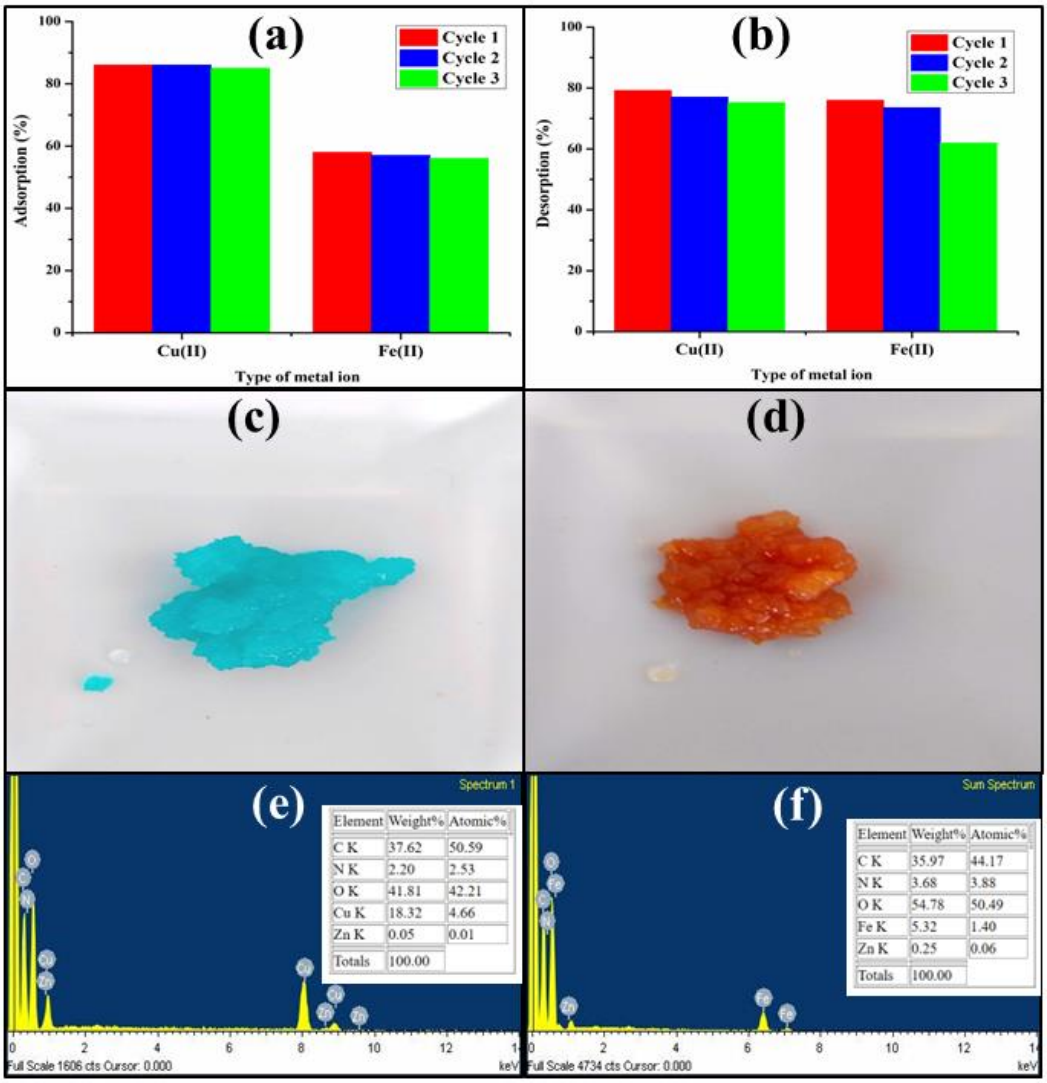

Figure 5.8. (a) Adsorption and (b) desorption percentages of Cu(II) and Fe(II) during three cycles (Adsorbent dose: 0.01g, time: 30 min, pH: 7, metal ion concentration: 20 ppm, volume: 50 mL); digital photographs of HNC2 after adsorption of (c) Cu(II) and (d) Fe(II) ions and EDX spectra of HNC2 after (e) Cu(II) and (f) Fe(II) ions adsorption.

Furthermore, to study the adsorption of Cu(II) and Fe(II) ions on the surface of HNC2, digital images were taken after adsorption of metal ions (shown in **Figure 5.8.(c** and **d)**, respectively). Additionally, EDX analysis was used to demonstrate the adsorption of metal ions onto the HNC2. Comparing the EDX spectra of the HNC2 adsorbent before adsorption (**Figure 5.3.b.**) and after adsorption (**Figure 5.8.e.**) for Cu(II) and **Figure**

5.8(f) for Fe(II)), it can be seen that the EDX spectrum of the adsorbent after adsorption is associated with new peaks corresponding to copper and iron elements, respectively.

5.3.9. Biodegradation

To understand the degradation profile of the prepared HNCs, a soil burial test was performed. The biodegradation rates of HNC0 and HNC2 for 35 days are given **Figure 5.9**. The figure shows that both the samples exhibited biodegradable properties due to the presence of high bio-content in the polymer matrix, which assisted with microbial attack. However, a slower weight loss rate was observed with HNC2 compared to HNC0. This may be due to the presence of ZO NPs which resist HNC2 from degradation due to the antibacterial properties [39].

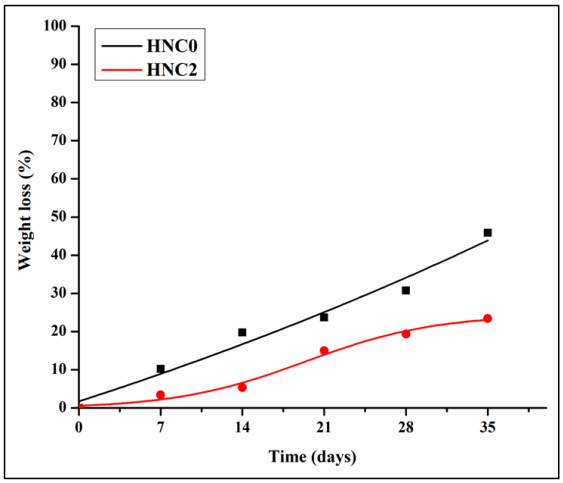

Figure 5.9. Weight loss (%) curve of HNC0 and HNC2 over 35 days of biodegradation.

5.4. Conclusion

In this work, a facile method was adopted to fabricate a mCNF and ZO-based nanohybrid and subsequently incorporated into the starch-based hydrogel. From various structural and morphological analysis, the preparation and incorporation of nanohybrid into the hydrogel matrix was observed. The prepared HNC was successfully used to adsorb Cu(II) and Fe(II) ions from their respective salt solutions and showed metal ion removal capacities of 122 and 70 mg/g, respectively, for Cu(II) and Fe(II) ions. Moreover, maximum water swelling capacity of 580 g/g was observed when 0.25 wt% of nanohybrid was incorporated. From kinetic and isotherm studies, the metal ion adsorption data were found to be fitted well with the PSO kinetic and Freundlich adsorption isotherm models. Besides, the hydrogel can be reused for up to three repeated cycles without significant loss of its efficiency. In addition to this, the hydrogel was

biodegradable as supported by soil burial method. Thus, the synthetic route provides a bio-based biodegradable hydrogel nanocomposite with excellent metal ion adsorption capacity with high recyclability. In summary, this research work provides a novel HNC for metal ions removal from the industrial wastewater as well as ground water to make water useful for drinking and other purpose. Moreover, the hydrogel can be also used to remove toxic pollutants including pharmaceuticals, pesticides from wastewater as well as it can be used as photocatalyst for dye degradation and biomedical applications due to the antibacterial activity of ZO NPs. Thus, this work opens up the most beneficial way to use the HNC for different application fields.

References

[1] Li, B. and Yin, H. Superior adsorption property of a novel green biosorbent yttrium/alginate gel beads for dyes from aqueous solution. *Journal of Polymers and the Environment*, 28:2137-2148, 2020.

[2] Zhang, W., Hu, L., Hu, S., and Liu, Y. Optimized synthesis of novel hydrogel for the adsorption of copper and cobalt ions in wastewater. *RSC Advances*, 9:16058-16068, 2019.

[3] Wang, G., Xiao, H., Liang, G., Zhu, J., He, C., Ma, S., Shuai, Z., and Komarneni, S. Leaching characteristics and stabilization of heavy metals in tin-polymetallic tailings by sodium diethyl dithiocarbamate intercalated montmorillonite (DDTC-Mt). *Journal of Cleaner Production*, 344:131041, 2020.

[4] Deng, S., Long, J., Dai, X., Wang, G., and Zhou, L. Simultaneous detection and adsorptive removal of Cr(VI) ions by fluorescent sulfur quantum dots embedded in chitosan hydrogels. *ACS Applied Nano Materials*, 6:1817-1827, 2023.

[5] Dutta, S., Gupta, B., Srivastava, S. K., and Gupta, A. K. Recent advances on the removal of dyes from wastewater using various adsorbents: A critical review. *Materials Advances*, 2:4497-4531, 2021.

[6] Ochedi, F. O., Liu, Y., and Hussain, A. A review on coal fly ash-based adsorbents for mercury and arsenic removal. *Journal of Cleaner Production*, 267:122143, 2020.

[7] Ramola, S., Belwal, T., Li, C. J., Liu, Y. X., Wang, Y. Y., Yang, S. M., and Zhou, C. H. Preparation and application of novel rice husk biochar–calcite

composites for phosphate removal from aqueous medium. *Journal of Cleaner Production*, 299:126802, 2021.

[8] Balasubramaniam, B., Prateek, Ranjan, S., Saraf, M., Kar, P., Singh, S. P., Thakur, V. K., Singh, A., and Gupta, R. K. Antibacterial and antiviral functional materials: Chemistry and biological activity toward tackling COVID-19-like pandemics. *ACS Pharmacology and Translational Science*, 4:8-54, 2020.

[9] Farooq, A., Patoary, M. K., Zhang, M., Mussana, H., Li, M., Naeem, M. A., and Liu, L. Cellulose from sources to nanocellulose and an overview of synthesis and properties of nanocellulose/zinc oxide nanocomposite materials. *International Journal of Biological Macromolecules*, 154:1050-1073, 2020.

[10] Patel, D. K., Dutta, S. D., and Lim, K. T. Nanocellulose-based polymer hybrids and their emerging applications in biomedical engineering and water purification. *RSC Advances*, 9:19143-19162, 2019.

[11] Zhan, W., Gao, L., Fu, X., Siyal, S. H., Sui, G., and Yang, X. Green synthesis of amino-functionalized carbon nanotube-graphene hybrid aerogels for high performance heavy metal ions removal. *Applied Surface Science*, 467:1122-1133, 2019.

[12] Fahimi-Kashani, N., Orouji, A., Ghamsari, M., Sahoo, S. K., and Hormozi-Nezhad, M. R. Plasmonic noble metal (Ag and Au) nanoparticles: From basics to colorimetric sensing applications. In *Gold and Silver Nanoparticles*, Pages 1-58. Elsevier, 2023.

[13] Abdalkarim, S. Y. H., Chen, L. M., Yu, H. Y., Li, F., Chen, X., Zhou, Y., and Tam, K. C. Versatile nanocellulose-based nanohybrids: A promising-new class for active packaging applications. *International Journal of Biological Macromolecules*, 182:1915-1930, 2021.

[14] Yedurkar, S., Maurya, C., and Mahanwar, P. Biosynthesis of zinc oxide nanoparticles using *Ixora coccinea* leaf extract—A green approach. *Open Journal of Synthesis Theory and Applications*, 5:1-14, 2016.

[15] Duarah, R. and Karak, N. Hyperbranched polyurethane/reduced carbon dot-zinc oxide nanocomposite-mediated solar-assisted photocatalytic degradation of organic contaminant: An approach towards environmental remediation. *Chemical Engineering Journal*, 370:716-728, 2019.

[16] Shah, L. A., Khan, M., Javed, R., Sayed, M., Khan, M. S., Khan, A., and Ullah, M. Superabsorbent polymer hydrogels with good thermal and mechanical properties for removal of selected heavy metal ions. *Journal of Cleaner Production*, 201:78-87, 2018.

[17] Liu, X., Guan, J., Lai, G., Xu, Q., Bai, X., Wang, Z., and Cui, S. Stimuli-responsive adsorption behavior toward heavy metal ions based on comb polymer functionalized magnetic nanoparticles. *Journal of Cleaner Production*, 253:119915, 2020.

[18] Vieira, R. S. and Beppu, M. M. Dynamic and static adsorption and desorption of Hg(II) ions on chitosan membranes and spheres. *Water Research,* 40:1726-1734, 2006.

[19] Nasrollahzadeh, M., Atarod, M., Sajjadi, M., Sajadi, S. M., and Issaabadi, Z. Plant-mediated green synthesis of nanostructures: Mechanisms, characterization, and applications, In *Interface Science and Technology*, Pages 199-322. Elsevier, 2019.

[20] Alinavaz, S., Mahdavinia, G. R., Jafari, H., Hazrati, M., and Akbari, A. Hydroxyapatite (HA)-based hybrid bionanocomposite hydrogels: Ciprofloxacin delivery, release kinetics and antibacterial activity. *Journal of Molecular Structure*, 1225:129095, 2021.

[21] Muhammad, W., Ullah, N., Haroon, M., and Abbasi, B. H. Optical, morphological and biological analysis of zinc oxide nanoparticles (ZnO NPs) using *Papaver somniferum* L. *RSC Advances*, 9:29541-29548, 2019.

[22] Quadri, T. W., Olasunkanmi, L. O., Fayemi, O. E., Solomon, M. M., and Ebenso, E. E. Zinc oxide nanocomposites of selected polymers: Synthesis, characterization, and corrosion inhibition studies on mild steel in HCl solution. *ACS Omega,* 2:8421-8437, 2017.

[23] Hosseini-Koupaei, M., Shareghi, B., Saboury, A. A., Davar, F., Sirotkin, V. A., Hosseini-Koupaei, M. H., and Enteshari, Z. Catalytic activity, structure and stability of proteinase K in the presence of biosynthesized CuO nanoparticles. *International Journal of Biological Macromolecules,* 122:732-744, 2019.

[24] Sen, S., Singh, A., Kailasam, K., Bera, C., and Roy, S. Biomass-derived cellulose nanofibers and iron oxide-based nanohybrids for thermal insulation application. *Nanoscale Advances,* 4:3381-3390, 2022.

[25] Javed, R., Shah, L. A., Sayed, M., and Khan, M. S. Uptake of heavy metal ions from aqueous media by hydrogels and their conversion to nanoparticles for generation of a catalyst system: Two-fold application study. *RSC Advances*, 8:14787-14797, 2018.

[26] George, D., Maheswari, P. U., Sheriffa Begum, K. M. M., and Arthanareeswaran, G. Biomass-derived dialdehyde cellulose cross-linked chitosan-based nanocomposite hydrogel with phytosynthesized zinc oxide nanoparticles for enhanced curcumin delivery and bioactivity. *Journal of Agricultural and Food Chemistry*, 67:10880-10890, 2019.

[27] Barzinjy, A. A. and Azeez, H. H. Green synthesis and characterization of zinc oxide nanoparticles using *Eucalyptus globulus* Labill. leaf extract and zinc nitrate hexahydrate salt. *SN Applied Sciences*, 2:991, 2020.

[28] Koupaei, M. H., Shareghi, B., Saboury, A. A., Davar, F., Semnani, A., and Evini, M. Green synthesis of zinc oxide nanoparticles and their effect on the stability and activity of proteinase K. *RSC Advances*, 6:42313-42323, 2016.

[29] Yang, R. T., Yu, H. Y., Song, M. L., Zhou, Y. W., and Yao, J. M. Flower-like zinc oxide nanorod clusters grown on spherical cellulose nanocrystals via simple chemical precipitation method. *Cellulose*, 23:1871-1884, 2016.

[30] Zheng, X., Wu, D., Su, T., Bao, S., Liao, C., and Wang, Q. Magnetic nanocomposite hydrogel prepared by ZnO-initiated photopolymerization for La(III) adsorption. *ACS Applied Materials and Interfaces*, 6:19840-19849, 2014.

[31] Wang, Y., Zhang, P., Liu, C. F., and Huang, C. Z. A facile and green method to fabricate graphene-based multifunctional hydrogels for miniature-scale water purification. *RSC Advances*, 3:9240-9246, 2013.

[32] Liu, J., Chu, H., Wei, H., Zhu, H., Wang, G., Zhu, J., and He, J. Facile fabrication of carboxymethyl cellulose sodium/graphene oxide hydrogel microparticles for water purification. *RSC Advances*, 6:50061-50069, 2016.

[33] Hassan, H., Salama, A., El-Ziaty, A. K., and El-Sakhawy, M. New chitosan/silica/zinc oxide nanocomposite as adsorbent for dye removal. *International Journal Biological Macromolecules*, 131:520-526, 2019.

[34] Dil, N. N. and Sadeghi, M. Free radical synthesis of nanosilver/gelatin-poly(acrylic acid) nanocomposite hydrogels employed for antibacterial activity and removal of Cu(II) metal ions. *Journal of Hazardous Materials*, 351:38-53, 2018.

[35] Senthil Kumar, P. Adsorption of lead(II) ions from simulated wastewater using natural waste: A kinetic, thermodynamic and equilibrium study. *Environmental Progress and Sustainable Energy*, 33:55-64, 2014.

[36] Ragheb, E., Shamsipur, M., Jalali, F., and Mousavi, F. Modified magnetic-metal organic framework as a green and efficient adsorbent for removal of heavy metals. *Journal of Environmental Chemical Engineering*, 10:107297, 2022.

[37] Ansari, R., Alizadeh, N., and Shademan, S. M. Application of silica gel/polyaniline composite for adsorption of ascorbic acid from aqueous solutions. *Iranian Polymer Journal*, 22:739-748, 2013.

[38] Saber-Samandari, S., Gulcan, H. O., Saber-Samandari, S., and Gazi, M. Efficient removal of anionic and cationic dyes from an aqueous solution using pullulan-graft-polyacrylamide porous hydrogel. *Water, Air and Soil Pollution*, 225:1-14, 2014.

[39] Patil, M. B., Rajamani, S. B., Mathad, S. N., Patil, A. Y., Hussain, M. A., Alorfii, H. S., and Puttegowda, M. Microwave-assisted synthesis of poly(acrylamide-co-2-hydroxyethyl methacrylate)/chitosan semi-IPN ZnO nanocomposite membranes for food packaging applications. *Journal of Materials Research and Technology*, 20:3537-3548, 2022.